A Combination Method of ROI, CLAHE, and DenseNet-169 for Hip Osteoarthritis Detection

Faisal Muttaqin
Information System Doctoral Program, School of Postgraduates Studies, Diponegoro University, Semarang, Central Java, Indonesia | Department of Informatics, Faculty of Computer Science, University of Pembangunan Nasional Veteran Jawa Timur, Surabaya, East Java, Indonesia
faisalmuttaqin9669@students.undip.ac.id (corresponding author)

Paulus Rahardjo
Radiology Department, Faculty of Medicine, Universitas Airlangga, Surabaya, Indonesia
paulus.r.rahardjo@gmail.com

Muhammad Zaim Chilmi
Orthopedic and Traumatology Department, Medical Faculty of Universitas Airlangga, Dr. Soetomo Hospital, Surabaya, East Java, Indonesia
m-zaid-chilmi@fk.unair.ac.id

Athanasius Priharyoto Bayuseno
Department of Mechanical Engineering, Faculty of Engineering, Diponegoro University, Semarang, 50275, Central Java, Indonesia
apbayuseno@lecturer.undip.ac.id

Tri Indah Winarni
Department of Anatomy, Faculty of Medicine, Diponegoro University, Semarang, 50275, Central Java, Indonesia | Undip Biomechanics Engineering & Research Center (UBM-ERC), Diponegoro University, Semarang, Central Java, Indonesia
triwinarni@lecturer.undip.ac.id

R. Rizal Isnanto
Department of Computer Engineering, Faculty of Engineering, Diponegoro University, Semarang, 50275, Central Java, Indonesia
rizal@lecturer.undip.ac.id

Jamari
Department of Mechanical Engineering, Faculty of Engineering, Diponegoro University, Semarang, Central Java, Indonesia | Undip Biomechanics Engineering & Research Center (UBM-ERC), Diponegoro University, Semarang, Central Java, Indonesia
j.jamari@gmail.com

Received: 15 February 2025 | Revised: 16 March 2025 | Accepted: 23 March 2025

 DOI: https://doi.org/10.48084/etasr.10576

ABSTRACT

Hip osteoarthritis is the second most persistent type of osteoarthritis after the knee, and one of its most common symptoms is discomfort in the afflicted joint. A previous study stated that 87.83% of patients undergoing hip arthroplasty were 60 years or older, with a higher prevalence among women, reflected in a 2:1 female-to-male ratio. Image enhancement is one of the most significant aspects of image processing, which, in addition to enhancing the clarity of visual images, is helpful for further analysis in the field of computer processing. This study employs a combination of techniques, specifically ROI (Region of

Interest), CLAHE (Contrast Limited Adaptive Histogram Equalization), and DenseNet-169. ROI is used to identify and define the specific area or object to be segmented. CLAHE is used to improve contrast in images, particularly those in grayscale, and DenseNet-169 is used for the detection of hip osteoarthritis. A total of 750 hip X-ray images were divided into 3 groups: 250 for normal osteoarthritis, 250 for mild osteoarthritis, and 250 for severe osteoarthritis. The proposed model obtained better scores than previous ones, with the following results: accuracy of 98.67%, precision of 98.70%, recall of 98.67%, and F1-score of 98.66%. These results show that the integration of ROI and CLAHE preprocessing techniques with DenseNet-169 effectively identifies hip osteoarthritis.

Keywords-image enhancement; deep learning; osteoarthritis; CLAHE; ROI; DenseNet-169

I. INTRODUCTION

Deep learning can resolve a wide range of challenging issues, including data analysis and computer vision [1, 2]. Deep learning is an artificial intelligence method that utilizes multilevel networks to learn features. Unlike machine learning, deep learning does not require manual feature extraction and instead trains a model from massive amounts of data, learning features, and performing classification or detection with sufficient data [3].

Osteoarthritis (OA) is a disease that affects joints and is caused by a complicated biological process that involves cartilage, muscle, bone, ligaments, synovium, and meniscus [4]. OA often occurs in older people [5, 6], but it can occur in middle-aged people [7]. In another explanation, OA is a degenerative joint condition that can destroy articular cartilage and structure [8]. OA can affect the knees, hips, hands, and spine [9, 10]. Hip OA is the second most persistent type of OA after the knee, with one of its most common symptoms being discomfort in the affected joint [11]. As stated in [12], 87.83% of the hip arthroplasty patients were 60 years or older, with a higher prevalence among women, reflected in a 2:1 female-to-male ratio. The Johnston County Osteoarthritis Project emphasizes the importance of further study on hip OA compared to knee OA, focusing on its prevalence and impact on morbidity and mortality [13].

The hip joint is shaped like a ball in a bowl, better known as a ball joint, and may move in several directions [14, 15]. From a biomechanical standpoint, the complicated movement could result in friction between the two bone surfaces that comprise the hip joint. When people age, they may develop a degenerative disease in their hip joint, known as primary hip OA [14, 16]. The advancement of image enhancement is a critical component of image processing development. In addition to enhancing the clarity of visual images, it is helpful for further analysis in computer processing [17-19].

This study uses a combination of methods, specifically ROI (Region of Interest), CLAHE (Contrast Limited Adaptive Histogram Equalization), and DenseNet-169. ROI is utilized to identify and define the specific area or object to be segmented. This section can encompass a particular object, a segment of the image, or a region that exhibits distinct characteristics. CLAHE is employed to improve contrast in images, particularly those in grayscale [20]. Meanwhile, DenseNet-169 is employed for the detection of hip OA. DenseNet is a Convolutional Neural Network (CNN) architecture to overcome the gradient vanishing issue [21-23]. The contributions of this study are as follows:

- Combines DenseNet-169 with ROI and CLAHE to detect hip OA.
- Achieves higher accuracy than that reported in previous studies.

II. RELATED WORKS

In [24], a deep-learning model was used to identify hip dysplasia using routine radiographs and classify dysplastic hips based on severity. ImageNet VGG16 underwent layer-by-layer fine-tuning and achieved an accuracy of 92.2% in differentiating normal and dysplastic hips, demonstrating significant promise. In [25], an automated hip radiography workflow was proposed for the prognosis of hip OA. A prediction model was developed and validated utilizing basic demographic data, physical examination, and radiological scores. The prediction results had an AUC of 0.795 at 95% CI (0.757-0.834). After incorporating the shape score, it reached an AUC of 0.864 at 95% CI (0.833-0.895), improving hip OA risk prediction. In [26] ResNet 18 was used to identify hip OA on clinical CT scans. Five different models were used, with models 3 and 5 achieving the best accuracy of 82.2%. This study showed that CT-based images that are analogous to radiography can be utilized to diagnose hip OA. Therefore, if there is a lack of substantial training data, deep learning methods can be optimized by combining CT-AP and X-ray images.

In [27], a computer-aided diagnostic approach was developed to assist physicians in diagnosing hip OA through the interpretation of standard hip radiographs. The VGG16 model was used on a dataset with 221 normal hip radiographs and 213 hip radiographs with OA. The results showed accuracy, sensitivity, specificity, and precision of 90.2%, 97.6%, 83.0%, and 84.7%, respectively. In [28], a multitask deep learning model based on DenseNet-161 was developed and validated in autonomously extracting radiographic characteristics of hip OA, particularly subchondral cysts, subchondral sclerosis, Femoral Osteophytes (FO), Joint Space Narrowing (JSN), and Acetabular Osteophytes (AO). The performance of the model was compared to that of musculoskeletal radiologists. The proposed model yielded different accuracies for the internal test, specifically: FO at 86.7%, AO at 69.9%, JSN at 81.7%, subchondral sclerosis at 95.8%, and subchondral cysts at 97.6%. The accuracy results for the external test set were the following: FO at 82.7%, AO at 65.4%, JSN at 80.8%, subchondral sclerosis at 88.5%, and subchondral cysts at 21.3%. In [29], an initial investigation was carried out on the diagnostic utility of deep learning in the context of hip OA, utilizing a CNN with the VGG16

architecture. A total of 420 Anteroposterior (AP) hip X-ray images were used from Chaoyang Hospital in Beijing, China, and the proposed model had an accuracy of 92.8%, a sensitivity of 95.0%, and a specificity of 90.7%.

III. MATERIAL AND METHODS

A laptop with an Intel Core i7-12700H processor, NVIDIA GeForce RTX 3070Ti 8GB GDDR6 graphics (TGP 150W), and 2×8 GB SO-DIMM DDR5-4800 memory were used along with the Python programming language for computational tasks [19]. Python libraries used in this study include NumPy for numerical computations and array manipulation, Pandas for table-based data analysis, Matplotlib for data visualization, TensorFlow/Keras for deep learning, and OpenCV for image processing. Figure 1 shows the proposed research flow, which includes the following stages.

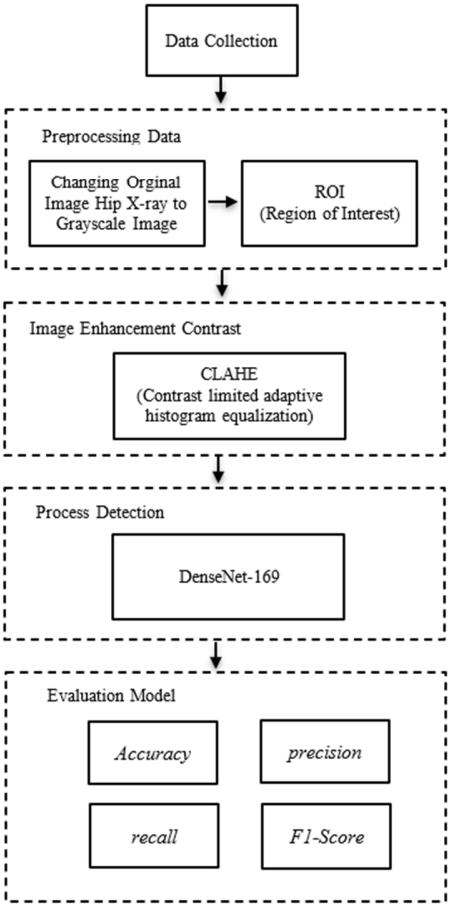

Fig. 1. Research flow.

A. Data Collection

This study involved X-ray images of hip joints from Dr. Sutomo Hospital in Surabaya by research permits and obtaining Ethics Clearance No. 1140/KEPK/X/2024. All X-ray image files in Dicom format that were acquired were subsequently transformed into PNG files [30] and then divided into two types of X-ray image, specifically the left hip and the right hip, as shown in Figure 2.

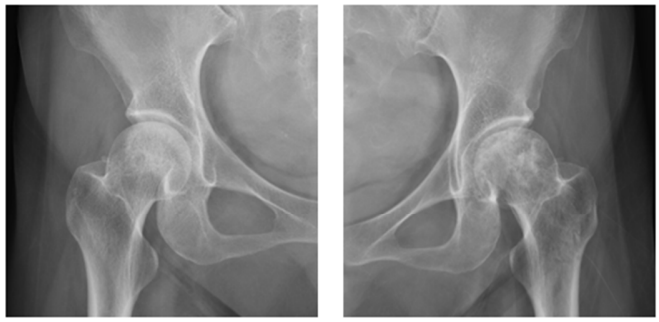

Fig. 2. Hip X-ray data sample.

Two radiologists who specialize in musculoskeletal imaging and have more than ten years of expertise were responsible for the process of reading the data from the hip X-ray images. A total of 750 hip X-ray images were obtained and divided into 3 groups, namely 250 for normal OA, 250 for mild OA, and 250 for severe OA.

B. Data Preprocessing

The X-ray images were transformed into grayscale. The following step involved the ROI procedure by identifying and deciding the region or item to segment. This section may comprise specific items, portions of the image, or sections with specific qualities. The ROI before image processing ensures that the region being processed focuses on the ROI rather than the entire frame [31]. According to [32], in the medical field, the ROI is of significant importance, as certain regions within an image possess a higher diagnostic value compared to others. Figure 3 shows an original and its ROI image.

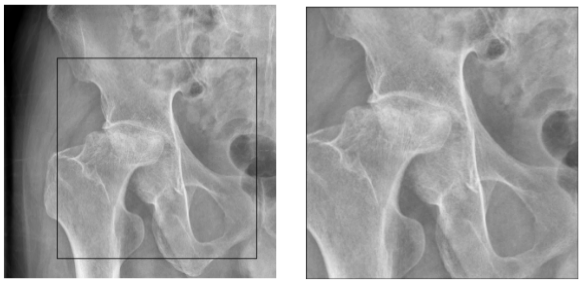

(a) (b)

Fig. 3. Hip X-ray: (a) Original image, (b) ROI image.

C. Image Enhancement

After preprocessing, each image advanced to the enhancement phase utilizing CLAHE, which is a technique to improve contrast in images, specifically those in grayscale [20]. CLAHE divides the image into tiles and applies histogram equalization to each tile. This increases the contrast in certain areas without changing the quality of the image as a whole [33]. CLAHE is suitable for images with different lighting situations since clip borders limit noise amplification [34].

CLAHE has been successfully implemented in MRI and X-ray imaging to make images clearer and diagnoses more accurate [33, 35]. The benefit of this procedure is that it can improve the quality of the original image, particularly

grayscale images, which are frequently used by medical workers for X-ray or CT scans and suffer from a high level of interference or noise [19]. Moreover, applying CLAHE to an image can enhance the accuracy of the results [36]. The CLAHE approach is defined as follows:

$$\beta = \frac{M}{N}\left(1 + \frac{\alpha}{100}(S_{max} - 1)\right) \quad (1)$$

where β signifies the limit value, M denotes the area size, N signifies the gray-level or grayscale value (256), and α represents the clip factor, which refers to the addition of the histogram limit with a value ranging from 1 to 100. S_{max} represents the maximum permissible slope. Figure 4 shows an original image and its CLAHE enhancement.

(a) (b)

Fig. 4. Hip X-ray: (a) Original image, (b) CLAHE image.

D. Detection Process

DenseNet-169 is a variant of the DenseNet architecture that includes 169 layers. DenseNet-169 was intentionally developed for picture-processing activities such as classification, object detection, and picture segmentation. The size of the input image was modified to match the model's anticipated size (224×224 pixels) [22, 27]. This architecture utilizes dense connections, enabling each layer to receive input from all preceding layers, improving feature propagation and reducing the vanishing gradient problem during training [37].

The DenseNet-169 design makes it possible to reuse features more effectively, which eventually leads to higher performance on complicated datasets, as demonstrated by the fact that a remote sensing application achieved an accuracy rate of 95.14% [38]. In the field of medicine, the DenseNet-169 architecture can also be utilized to identify, categorize, or diagnose a wide range of disorders, including the detection of pneumonia [39], the classification of lung cancer [40], and the diagnosis of CoViD-19 [41]. The DenseNet architecture has also been used to detect whether an image is real or fake [42].

E. Evaluation Model

Model evaluation uses metrics such as accuracy, precision, recall, and F1-score. The four terms utilized in the confusion matrix are True Positive (TP), True Negative (TN), False Positive (FP), and False Negative (FN).

- Accuracy measures the overall correctness of the model and is calculated as the ratio of correct predictions to the total number of cases examined. It provides a quick indication of how well the model performs across all classes.

$$Accuracy = \frac{Number\ of\ correct\ predictions}{Total\ number\ of\ predictions} \quad (2)$$

- Precision is used to calculate the positive predictions from all anticipated positive outcomes:

$$Precision = \frac{TP}{TP+FP} \quad (3)$$

- Recall or sensitivity measures the proportion of actual positives that are correctly identified as such. This is important for applications where missing positive predictions can be detrimental.

$$Recall\ or\ Sensitivity = \frac{TP}{TP+FN} \quad (4)$$

- F1-score is the harmonic mean or weighted comparison of average precision and recall. F1-score ranges from 0 to 1, signifying that the classification model has strong precision and recall.

$$F1 - score = 2 \times \frac{Precision \times Recall}{Precision + Recall} \quad (5)$$

IV. RESULTS AND DISCUSSION

The process involved several stages: converting the original image to grayscale, performing the ROI process, enhancing image contrast using CLAHE, and finally employing DenseNet-169 for hip OA detection. The dataset comprised a total of 750 entries, including 250 instances of normal OA, 250 instances of mild OA, and 250 instances of severe OA.

The dataset was partitioned into two primary sets: 70% (175) allocated for training and 30% (75) designated for testing. The training process was carried out using different epoch settings to assess the model performance in terms of variations in training parameters. The employed configurations are as follows:

- Configuration 1: The model is trained with 25 epochs.
- Configuration 2: The model is trained with 40 epochs.
- Configuration 3: The model is trained with 60 epochs.

The purpose of each configuration is to assess the impact of training length on predictive accuracy and performance. The last results of each configuration were examined to train the most effective model according to the evaluation metrics. The 'Image type' column in Tables I, II, and III indicates the number of sample trials displayed from the overall test dataset.

Table I presents the evaluation results with 25 epochs. The evaluation results in Table I indicate consistent model performance, with performance metric values between 0.92 and 0.95. The peak performance was observed with 0.9556 accuracy, 0.9570 precision, 0.9556 recall, and 0.9555 F1-score, indicating that the model had maximal efficacy in the trial. In contrast, the lowest performance recorded a 0.9244 accuracy, 0.9251 precision, 0.9244 recall, and 0.9238 F1-score, indicating commendable results. Furthermore, the equilibrium among precision, recall, and F1-score indicates that the model effectively minimizes prediction errors, including both FP and FN.

TABLE I. RESULTS WITH 25 EPOCHS

Image type	Prediction results			
	Accuracy	Precision	Recall	F1-score
Normal OA 1	0.9378	0.9381	0.9378	0.9373
Normal OA 2	0.9467	0.9474	0.9467	0.9465
Normal OA 3	0.9289	0.9283	0.9289	0.9283
Normal OA 4	0.9378	0.9379	0.9378	0.9373
Normal OA 5	0.9333	0.9333	0.9333	0.9328
Mild OA 1	0.9467	0.9473	0.9467	0.9464
Mild OA 2	0.9333	0.9353	0.9333	0.9330
Mild OA 3	0.9289	0.9283	0.9289	0.9283
Mild OA 4	0.9467	0.9473	0.9467	0.9464
Mild OA 5	0.9422	0.9422	0.9422	0.9419
Severe OA 1	0.9422	0.9424	0.9422	0.9419
Severe OA 2	0.9333	0.9338	0.9333	0.9328
Severe OA 3	0.9556	0.9570	0.9556	0.9555
Severe OA 4	0.9378	0.9397	0.9378	0.9375
Severe OA 5	0.9244	0.9251	0.9244	0.9238

Overall, the variation in the results between experiments tends to be small, reflecting the stability of the model. This indicates that the model exhibits low sensitivity to random variables and possesses commendable generalization capability. Figures 5 (model accuracy) and 6 (model loss) illustrate the graphs representing the comprehensive evaluation findings of the configuration with 25 epochs.

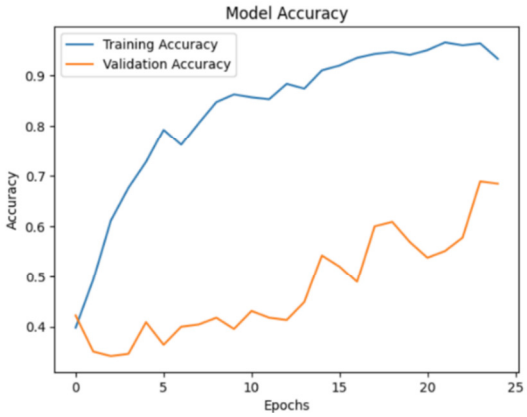

Fig. 5. Model accuracy with 25 epochs.

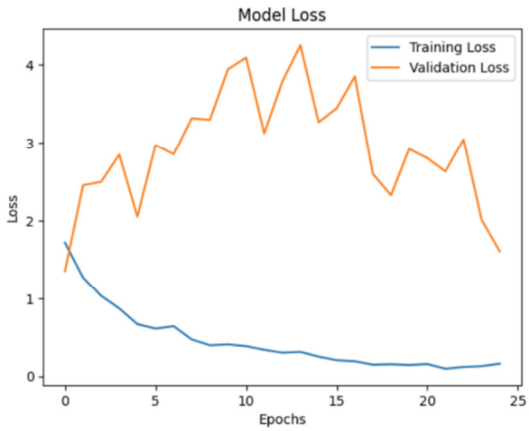

Fig. 6. Model loss with 25 epochs.

Table II shows the evaluation results of the configuration with 40 epochs.

TABLE II. RESULTS WITH 40 EPOCHS

Image type	Prediction results			
	Accuracy	Precision	Recall	F1-Score
Normal OA 1	0.7778	0.8193	0.7778	0.7599
Normal OA 2	0.8267	0.8781	0.8267	0.8154
Normal OA 3	0.8178	0.8598	0.8178	0.8073
Normal OA 4	0.7778	0.8162	0.7778	0.7625
Normal OA 5	0.7911	0.8311	0.7911	0.7776
Mild OA 1	0.7867	0.8470	0.7867	0.7657
Mild OA 2	0.7867	0.8318	0.7867	0.7694
Mild OA 3	0.7911	0.8442	0.7911	0.7742
Mild OA 4	0.8178	0.8598	0.8178	0.8073
Mild OA 5	0.8000	0.8429	0.8000	0.7870
Severe OA 1	0.8133	0.8778	0.8133	0.7966
Severe OA 2	0.8000	0.8320	0.8000	0.7898
Severe OA 3	0.8089	0.8485	0.8089	0.7979
Severe OA 4	0.8000	0.8543	0.8000	0.7830
Severe OA 5	0.7867	0.8389	0.7867	0.7676

The results in Table II demonstrate a performance that is pretty satisfactory and consistent with the primary metrics. The model was trained for 40 epochs and achieved accuracy ranging from 0.7778 to 0.8267, precision ranging from 0.8162 to 0.8781, recall ranging from 0.7778 to 0.8267, and F1-score ranging from 0.7599 to 0.8154 on average. The highest performance was achieved in the second row, which is associated with normal OA, with an accuracy of 0.8267, a precision of 0.8781, a recall of 0.8267, and an F1-score of 0.8154, indicating that there is a perfect equilibrium between the ability to recognize positive data and the accuracy of the results. On the other hand, the first row associated with normal OA represents the lowest performance, with an accuracy of 0.7778, a precision of 0.8193, a recall of 0.7778, and an F1-score of 0.7599. However, this result continues to be larger than the average, which is indicative of the model's general consistency.

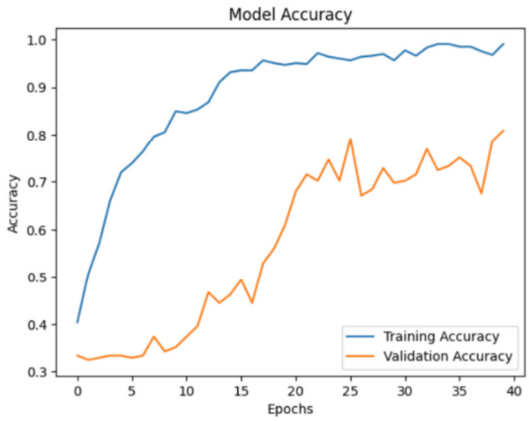

Fig. 7. Model accuracy with 40 epochs.

The correlation across metrics indicates that precision and recall mutually reinforce one another with some minor variations, whereas the F1-score exemplifies the equilibrium

between them. To improve performance, more optimization of recall is required through bias mitigation, supplementary validation with novel data to ensure generalization, and hyperparameter adjustment to address suboptimal performance outcomes. Overall, the model demonstrated encouraging results. Figures 7 (model accuracy) and 8 (model loss) illustrate the graphs showing the comprehensive evaluation results of the model with 40 epochs.

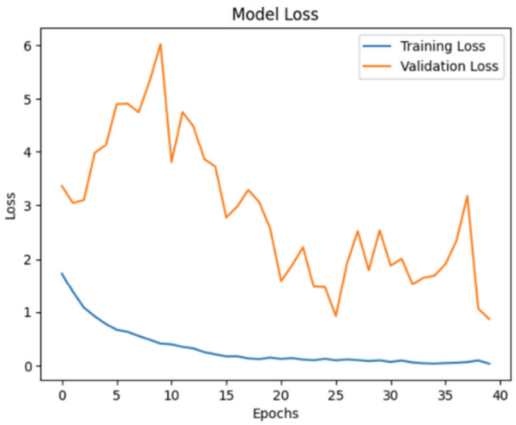

Fig. 8. Model loss with 40 epochs.

Table III shows the evaluation results of the model with 60 epochs.

TABLE III. RESULTS WITH 60 EPOCHS

Image type	Prediction results			
	Accuracy	Precision	Recall	F1-score
Normal OA 1	0.9644	0.9679	0.9644	0.9643
Normal OA 2	0.9733	0.9748	0.9733	0.9732
Normal OA 3	0.9822	0.9822	0.9822	0.9822
Normal OA 4	0.9600	0.9635	0.9600	0.9596
Normal OA 5	0.9867	0.9870	0.9867	0.9866
Mild OA 1	0.9689	0.9715	0.9689	0.9688
Mild OA 2	0.9689	0.9705	0.9689	0.9685
Mild OA 3	0.9778	0.9792	0.9778	0.9778
Mild OA 4	0.9778	0.9787	0.9778	0.9776
Mild OA 5	0.9867	0.9872	0.9867	0.9867
Severe OA 1	0.9689	0.9709	0.9689	0.9687
Severe OA 2	0.9733	0.9748	0.9733	0.9732
Severe OA 3	0.9644	0.9672	0.9644	0.9642
Severe OA 4	0.9822	0.9831	0.9822	0.9822
Severe OA 5	0.9778	0.9785	0.9778	0.9776

The results in Table III demonstrate the model's performance after training for a total of 60 epochs. The findings demonstrate consistently high performance, with accuracy values ranging from 0.9600 to 0.9867, precision from 0.9635 to 0.9872, recall from 0.9600 to 0.9867, and F1-score from 0.9596 to 0.9867. The model demonstrates a commendable equilibrium between precision and recall, as evidenced by the consistent F1-score values across almost all rows. The highest performance was achieved with an accuracy of 0.9867, while the lowest performance was observed with an accuracy of 0.9600. Figures 9 (model accuracy) and 10 (model loss) present graphs depicting the comprehensive evaluation findings of the model trained for 60 epochs.

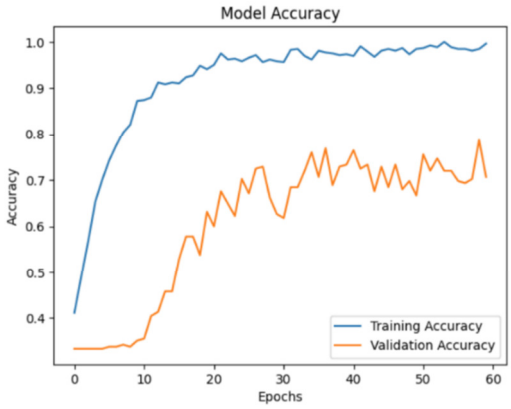

Fig. 9. Model accuracy with 60 epochs.

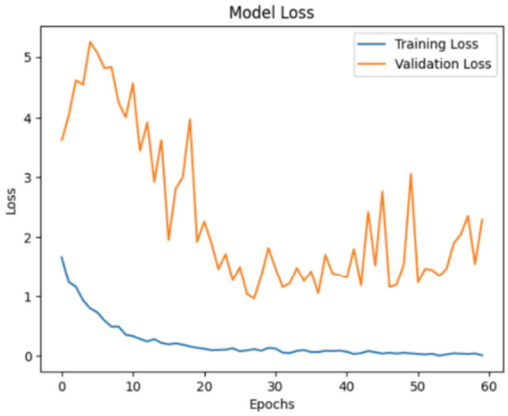

Fig. 10. Model loss with 60 epochs.

Several preventive measures can be taken in the case of overfitting. One method is regularization, which involves adding a penalty to prevent the model from becoming overly complex. Another approach is dropout, which randomly deactivates certain parts of the neural network during training to prevent the model from relying too heavily on specific patterns. Early stopping can also be applied, where the training process is halted early if performance on validation data no longer improves. Additionally, data augmentation, such as rotating, zooming, or adding noise to images, helps the model learn from a wider variety of data.

The findings of this study were compared with those of earlier studies, as shown in Table IV.

TABLE IV. COMPARISON WITH PREVIOUS STUDIES

Study	Method	Dataset size	Evaluation results
[24]	CNN (VGG16)	571	Accuracy = 92.2%
[27]	CNN (VGG16)	434	Accuracy = 90.2% Precision = 84.7% Recall = 97.6% Specificity = 83%
This model	CNN (DenseNet-169), ROI, and CLAHE	750	Accuracy = 98.67% Precision = 98.70% Recall = 98.67% F1-score = 98.66%

As shown in Table IV, in [27], a computer aided diagnosis method was developed to assist physicians in diagnosing hip osteoarthritis by interpreting plain pelvic radiographs using VGG16. Using a dataset of 434 images, the model achieved an accuracy of 90.2%, precision of 84.7%, recall of 97.6%, and specificity of 83%. In [24], a deep learning model was developed to diagnose hip dysplasia from plain radiographs and classify dysplastic hips based on severity, using VGG16 with a dataset of 571 images, resulting in an accuracy of 92.2%. The proposed model using DenseNet-169 and enhanced with additional ROI and CLAHE techniques achieved an accuracy of 98.67%, a precision of 98.70%, a recall of 98.67%, and an F1-Score of 98.66% on a dataset of 750 images. The results of this study demonstrate that the DenseNet-169 approach, when combined with supplementary techniques, achieves optimal performance, evidenced by the highest accuracy and recall of 98.67%. This finding confirms that the integration of ROI and CLAHE preprocessing methods with DenseNet-169 effectively detects hip OA.

V. CONCLUSION

This study applies a CNN with DenseNet-169 architecture, incorporating preprocessing techniques such as ROI and CLAHE to detect hip osteoarthritis. The test findings indicate that the proposed method outperforms previous approaches, achieving an accuracy of 98.67%, a precision of 98.70%, a recall of 98.67%, and an F1-score of 98.66%. These results show that the integration of ROI and CLAHE preprocessing techniques with DenseNet-169 effectively identifies hip OA.

REFERENCES

[1] C. M. Lo and K. L. Lai, "Deep learning-based assessment of knee septic arthritis using transformer features in sonographic modalities," *Computer Methods and Programs in Biomedicine*, vol. 237, Jul. 2023, Art. no. 107575, https://doi.org/10.1016/j.cmpb.2023.107575.

[2] R. Khan *et al.*, "Comparative study of deep learning techniques for DeepFake video detection," *ICT Express*, vol. 10, no. 6, pp. 1226–1239, Dec. 2024, https://doi.org/10.1016/j.icte.2024.09.018.

[3] C. Huang, J. Wang, S. Wang, and Y. Zhang, "A review of deep learning in dentistry," *Neurocomputing*, vol. 554, Oct. 2023, Art. no. 126629, https://doi.org/10.1016/j.neucom.2023.126629.

[4] R. S. Hinman, M. Hall, S. Comensoli, and K. L. Bennell, "Exercise & Sports Science Australia (ESSA) updated Position Statement on exercise and physical activity for people with hip/knee osteoarthritis," *Journal of Science and Medicine in Sport*, vol. 26, no. 1, pp. 37–45, Jan. 2023, https://doi.org/10.1016/j.jsams.2022.11.003.

[5] S. Wang *et al.*, "Identification of several inflammation-related genes based on bioinformatics and experiments," *International Immunopharmacology*, vol. 121, Aug. 2023, Art. no. 110409, https://doi.org/10.1016/j.intimp.2023.110409.

[6] J. Li, C. N. Lan, Y. Kong, S. S. Feng, and T. Huang, "Identification and Analysis of Blood Gene Expression Signature for Osteoarthritis With Advanced Feature Selection Methods," *Frontiers in Genetics*, vol. 9, Aug. 2018, Art. no. 246, https://doi.org/10.3389/fgene.2018.00246.

[7] J. Meng, H. Du, H. Lv, J. Lu, J. Li, and J. Yao, "Identification of the osteoarthritis signature gene PDK1 by machine learning and its regulatory mechanisms on chondrocyte autophagy and apoptosis," *Frontiers in Immunology*, vol. 13, Jan. 2023, Art. no. 1072526, https://doi.org/10.3389/fimmu.2022.1072526.

[8] N. Aresti, J. Kassam, N. Nicholas, and P. Achan, "Hip osteoarthritis," *BMJ*, Jul. 2016, Art. no. i3405, https://doi.org/10.1136/bmj.i3405.

[9] R. T. Wahyuningrum, L. Anifah, I. K. Eddy Purnama, and M. Hery Purnomo, "A New Approach to Classify Knee Osteoarthritis Severity from Radiographic Images based on CNN-LSTM Method," in *2019 IEEE 10th International Conference on Awareness Science and Technology (iCAST)*, Morioka, Japan, Oct. 2019, pp. 1–6, https://doi.org/10.1109/ICAwST.2019.8923284.

[10] D. Prieto-Alhambra, A. Judge, M. K. Javaid, C. Cooper, A. Diez-Perez, and N. K. Arden, "Incidence and risk factors for clinically diagnosed knee, hip and hand osteoarthritis: influences of age, gender and osteoarthritis affecting other joints," *Annals of the Rheumatic Diseases*, vol. 73, no. 9, pp. 1659–1664, Sep. 2014, https://doi.org/10.1136/annrheumdis-2013-203355.

[11] N. Veronese *et al.*, "Association between lower limb osteoarthritis and incidence of depressive symptoms: data from the osteoarthritis initiative," *Age and Ageing*, vol. 46, no. 3, pp. 470–476, May 2017, https://doi.org/10.1093/ageing/afw216.

[12] A. T. Paraliov, Ş. Crăiţoiu, M. M. Iacov-Craitoiu, and L. Mogoantă, "Hip Osteoarthritis-Clinical-Statistical Study and Surgical Treatment," *Current Health Sciences Journal*, vol. 50, no. 2, pp. 246–255, Jul. 2024, https://doi.org/10.12865/CHSJ.50.02.10.

[13] A. Nelson, "Epidemiology of Hip Osteoarthritis: The Johnston County Osteoarthritis Project," *HSS Journal®: The Musculoskeletal Journal of Hospital for Special Surgery*, vol. 19, no. 4, pp. 413–417, Nov. 2023, https://doi.org/10.1177/15563316231192372.

[14] M. Sangeux, "Biomechanics of the Hip During Gait," in *The Pediatric and Adolescent Hip*, S. Alshryda, J. J. Howard, J. S. Huntley, and J. G. Schoenecker, Eds. Springer International Publishing, 2019, pp. 53–71.

[15] D. P. Byrne, K. J. Mulhall, and J. F. Baker, "Anatomy & Biomechanics of the Hip," *The Open Sports Medicine Journal*, vol. 4, no. 1, pp. 51–57, Jan. 2010, https://doi.org/10.2174/1874387001004010051.

[16] M. D. Harris, "The Geometry And Biomechanics Of Normal And Pathomorphologic Human Hips," Ph.D. dissertation, University of Utah, USA, 2013.

[17] J. Yang and S. Xuan, "Bit depth enhancement method for low-contrast images based on sequence image fusion," *Measurement: Sensors*, vol. 27, Jun. 2023, Art. no. 100801, https://doi.org/10.1016/j.measen.2023.100801.

[18] N. Senthilkumaran and J. Thimmiaraja, "Histogram Equalization for Image Enhancement Using MRI Brain Images," in *2014 World Congress on Computing and Communication Technologies*, Trichirappalli, India, Feb. 2014, pp. 80–83, https://doi.org/10.1109/WCCCT.2014.45.

[19] F. Muttaqin, R. R. Isnanto, T. I. Winarni, and A. P. Bayuseno, "Application of Contrast Enhancement Method on Hip X-ray Images as a Media for Detecting Hip Osteoarthritis.," *International Journal of Advanced Computer Science & Applications*, vol. 15, no. 11, 2024.

[20] K. Honda, K. Wei, M. Arai, and H. Amano, "CLAHE Implementation and Evaluation on a Low-End FPGA Board by High-Level Synthesis," *IEICE Transactions on Information and Systems*, vol. E104.D, no. 12, pp. 2048–2056, Dec. 2021, https://doi.org/10.1587/transinf.2021PAP0006.

[21] R. K. Srivastava, K. Greff, and J. Schmidhuber, "Highway Networks." arXiv, Nov. 03, 2015, https://doi.org/10.48550/arXiv.1505.00387.

[22] G. Huang, Z. Liu, L. van der Maaten, and K. Q. Weinberger, "Densely Connected Convolutional Networks." arXiv, Jan. 28, 2018, https://doi.org/10.48550/arXiv.1608.06993.

[23] K. He, X. Zhang, S. Ren, and J. Sun, "Deep Residual Learning for Image Recognition." arXiv, Dec. 10, 2015, https://doi.org/10.48550/arXiv.1512.03385.

[24] M. Magnéli *et al.*, "Application of deep learning for automated diagnosis and classification of hip dysplasia on plain radiographs," *BMC Musculoskeletal Disorders*, vol. 25, no. 1, Feb. 2024, Art. no. 117, https://doi.org/10.1186/s12891-024-07244-0.

[25] W. P. Gielis *et al.*, "An automated workflow based on hip shape improves personalized risk prediction for hip osteoarthritis in the CHECK study," *Osteoarthritis and Cartilage*, vol. 28, no. 1, pp. 62–70, Jan. 2020, https://doi.org/10.1016/j.joca.2019.09.005.

[26] R. K. Gebre *et al.*, "Detecting hip osteoarthritis on clinical CT: a deep learning application based on 2-D summation images derived from CT," *Osteoporosis International*, vol. 33, no. 2, pp. 355–365, Feb. 2022, https://doi.org/10.1007/s00198-021-06130-y.

[27] K. Üreten, T. Arslan, K. E. Gültekin, A. N. D. Demir, H. F. Özer, and Y. Bilgili, "Detection of hip osteoarthritis by using plain pelvic radiographs with deep learning methods," *Skeletal Radiology*, vol. 49, no. 9, pp. 1369–1374, Sep. 2020, https://doi.org/10.1007/s00256-020-03433-9.

[28] C. E. Von Schacky *et al.*, "Development and Validation of a Multitask Deep Learning Model for Severity Grading of Hip Osteoarthritis Features on Radiographs," *Radiology*, vol. 295, no. 1, pp. 136–145, Apr. 2020, https://doi.org/10.1148/radiol.2020190925.

[29] Y. Xue, R. Zhang, Y. Deng, K. Chen, and T. Jiang, "A preliminary examination of the diagnostic value of deep learning in hip osteoarthritis," *PLOS ONE*, vol. 12, no. 6, Jun. 2017, Art. no. e0178992, https://doi.org/10.1371/journal.pone.0178992.

[30] S. Anand, R. K. Roshan, and D. Sundaram M, "Chest X ray image enhancement using deep contrast diffusion learning," *Optik*, vol. 279, May 2023, Art. no. 170751, https://doi.org/10.1016/j.ijleo.2023.170751.

[31] A. H. Pratomo, W. Kaswidjanti, and S. Mu'arifah, "Implementasi Algoritma Region of Interest (ROI) untuk Meningkatkan Performa Algoritma Deteksi dan Klasifikasi Kendaraan," *Jurnal Teknologi Informasi dan Ilmu Komputer*, vol. 7, no. 1, pp. 155–162, Feb. 2020.

[32] C. Doukas and I. Maglogiannis, "Region of Interest Coding Techniques for Medical Image Compression," *IEEE Engineering in Medicine and Biology Magazine*, vol. 26, no. 5, pp. 29–35, Sep. 2007, https://doi.org/10.1109/EMB.2007.901793.

[33] I. R. Swadi, T. F. Mahdi, and H. G. Daway, "MRI Image Enhancement Using Multilevel Image Thresholds Based on Contrast-limited Adaptive Histogram Equalization," *Iraqi Journal of Science*, pp. 5888–5899, Oct. 2024, https://doi.org/10.24996/ijs.2024.65.10.44.

[34] S. R. Borra, N. P. Tejaswini, V. Malathy, B. Magesh Kumar, and M. I. Habelalmateen, "Contrast Limited Adaptive Histogram Equalization based Multi-Objective Improved Cat Swarm Optimization for Image Contrast Enhancement," in *2023 International Conference on Integrated Intelligence and Communication Systems (ICIICS)*, Kalaburagi, India, Nov. 2023, pp. 1–5, https://doi.org/10.1109/ICIICS59993.2023.10420959.

[35] S. N. Nia and F. Y. Shih, "Medical X-Ray Image Enhancement Using Global Contrast-Limited Adaptive Histogram Equalization," *International Journal of Pattern Recognition and Artificial Intelligence*, vol. 38, no. 12, Sep. 2024, Art. no. 2457010, https://doi.org/10.1142/S0218001424570106.

[36] S. Phimphisan and N. Sriwiboon, "A Customized CNN Architecture with CLAHE for Multi-Stage Diabetic Retinopathy Classification," *Engineering, Technology & Applied Science Research*, vol. 14, no. 6, pp. 18258–18263, Dec. 2024, https://doi.org/10.48084/etasr.8932.

[37] M. H. P. A. Siddiqui, "DenseNet: Assessing Limitations in Connectivity and Memory Efficiency," *International Journal Of Scientific Research In Engineering And Management*, vol. 08, no. 10, pp. 1–7, Oct. 2024, https://doi.org/10.55041/IJSREM38175.

[38] C. Xiyue, "Remote sensing image scene recognition based on densenet-169," in *International Conference on Image, Signal Processing, and Pattern Recognition (ISPP 2024)*, Guangzhou, China, Jun. 2024, Art. no. 24, https://doi.org/10.1117/12.3033532.

[39] M. Bundea and G. M. Danciu, "Pneumonia Image Classification Using DenseNet Architecture," *Information*, vol. 15, no. 10, Oct. 2024, Art. no. 611, https://doi.org/10.3390/info15100611.

[40] S. Chaudhary, "Comparative Analysis of DenseNet Architectures for Lung Cancer Classification Using Histopathologic Images," *International Journal of Science and Engineering Applications*, Sep. 2024, https://doi.org/10.7753/IJSEA1309.1003.

[41] R. Rajpoot, M. Gour, S. Jain, and V. B. Semwal, "Integrated ensemble CNN and explainable AI for COVID-19 diagnosis from CT scan and X-ray images," *Scientific Reports*, vol. 14, no. 1, Oct. 2024, Art. no. 24985, https://doi.org/10.1038/s41598-024-75915-y.

[42] A. Alzahrani, "Digital Image Forensics: An Improved DenseNet Architecture for Forged Image Detection," *Engineering, Technology & Applied Science Research*, vol. 14, no. 2, pp. 13671–13680, Apr. 2024, https://doi.org/10.48084/etasr.7029.